# Enhancing nanostructured nickel-rich lithium-ion battery cathodes via surface stabilization Ⓕ

Jin-Myoung Lim, Norman S. Luu, Kyu-Young Park, Mark T. Z. Tan, Sungkyu Kim, Julia R. Downing, Kai He, ⓘD Vinayak P. Dravid, and ⓘD Mark C. Hersam

## COLLECTIONS

Paper published as part of the special topic on Celebrating 40 Years of the AVS Peter Mark Award

Ⓕ   This paper was selected as Featured

View Online          Export Citation          CrossMark

## ARTICLES YOU MAY BE INTERESTED IN

Unveiling the dimensionality effect of conductive fillers in thick battery electrodes for high-energy storage systems
Applied Physics Reviews **7**, 041405 (2020); https://doi.org/10.1063/5.0024123

Large-area optoelectronic-grade InSe thin films via controlled phase evolution
Applied Physics Reviews **7**, 041402 (2020); https://doi.org/10.1063/5.0023080

Plasma enhanced atomic layer deposition of thin film $Li_{1+x}Mn_{2-x}O_4$ for realization of all solid-state 3D lithium-ion microbatteries
Journal of Vacuum Science & Technology A **39**, 012408 (2021); https://doi.org/10.1116/6.0000644

# Enhancing nanostructured nickel-rich lithium-ion battery cathodes via surface stabilization (F)

View Online · Export Citation · CrossMark

Jin-Myoung Lim,[1] Norman S. Luu,[1] Kyu-Young Park,[1] Mark T. Z. Tan,[1] Sungkyu Kim,[1,2,3] Julia R. Downing,[1] Kai He,[1,2,4] Vinayak P. Dravid,[1,2] (iD) and Mark C. Hersam[1,5,6,a)] (iD)

## AFFILIATIONS

[1]Department of Materials Science and Engineering, Northwestern University, 2220 Campus Drive, Evanston, Illinois 60208
[2]NUANCE Center, Northwestern University, 2220 Campus Drive, Evanston, Illinois 60208
[3]HMC, Department of Nanotechnology and Advanced Materials Engineering, Sejong University, 209 Neungdong-ro, Gwangjin-gu, Seoul 05006, Republic of Korea
[4]Department of Materials Science and Engineering, Clemson University, 515 Calhoun Drive, Clemson, South Carolina 29634
[5]Department of Chemistry, Northwestern University, 2220 Campus Drive, Evanston, Illinois 60208
[6]Department of Electrical and Computer Engineering, Northwestern University, 2145 Sheridan Road, Evanston, Illinois 60208

**Note:** This paper is part of the 2020 Special Topic Collection Celebrating 40 Years of the AVS Peter Mark Award.
[a)]**Author to whom correspondence should be addressed:** m-hersam@northwestern.edu

## ABSTRACT

Layered, nickel-rich lithium transition metal oxides have emerged as leading candidates for lithium-ion battery (LIB) cathode materials. High-performance applications for nickel-rich cathodes, such as electric vehicles and grid-level energy storage, demand electrodes that deliver high power without compromising cell lifetimes or impedance. Nanoparticle-based nickel-rich cathodes seemingly present a solution to this challenge due to shorter lithium-ion diffusion lengths compared to incumbent micrometer-scale active material particles. However, since smaller particle sizes imply that surface effects become increasingly important, particle surface chemistry must be well characterized and controlled to achieve robust electrochemical properties. Moreover, residual surface impurities can disrupt commonly used carbon coating schemes, which result in compromised cell performance. Using x-ray photoelectron spectroscopy, here we present a detailed characterization of the surface chemistry of $LiNi_{0.8}Al_{0.15}Co_{0.05}O_2$ (NCA) nanoparticles, ultimately identifying surface impurities that limit LIB performance. With this chemical insight, annealing procedures are developed that minimize these surface impurities, thus improving electrochemical properties and enabling conformal graphene coatings that reduce cell impedance, maximize electrode packing density, and enhance cell lifetime fourfold. Overall, this work demonstrates that controlling and stabilizing surface chemistry enables the full potential of nanostructured nickel-rich cathodes to be realized in high-performance LIB technology.

## I. INTRODUCTION

As society transitions toward a renewable energy infrastructure, lithium-ion batteries (LIBs) have emerged as attractive power sources for key applications such as electric vehicles and consumer electronics. By tailoring the electrode materials, LIBs can be rationally designed to possess electrochemical properties that are customized for specific commercial technologies. For example, electric vehicles require high-power performance for fast acceleration, high-energy performance for long drivable range, and long cell lifetimes to minimize the need for cumbersome battery replacement.[1]

Consequently, significant efforts in LIB research have been focused on developing stable, high-capacity, and high-rate electrode materials.

Layered lithium transition metal oxides, especially nickel-rich chemistries such as $LiNi_{0.8}Al_{0.15}Co_{0.05}O_2$ (NCA), have emerged as leading LIB cathode material candidates due to their high operating potentials, high capacities, smooth voltage profiles, and facile synthesis.[1–3] However, the adoption of these materials in high-power commercial applications has been hindered by poor rate performance, which can partially be attributed to relatively slow

lithium-ion bulk diffusivities. Therefore, to achieve the high electrode power density and rate performance demanded by electric vehicles, a seemingly attractive strategy is to shrink the active material particle size to both decrease lithium-ion bulk diffusion lengths and increase the number of charge transfer sites.[4]

Despite the apparent advantages of nanoparticle-based LIB electrodes, this approach introduces its own unique challenges. In addition to difficulty in packing nanoparticles and conventional carbon black conductive additives into dense electrodes, the increased surface area associated with smaller particle sizes increases the severity of degradation mechanisms driven by surface impurities, which are found as by-products of materials synthesis and are generated as components of interfacial layers that form during electrochemical cycling. Indeed, the surface chemistries of electrochemically active materials are well-known to have significant implications for long-term stability.[5–11] Residual surface impurities are especially problematic for nickel-rich layered oxides,[9] suggesting that the active material surface chemistry needs to be carefully characterized and controlled in order to achieve high-performance nanoparticle-based LIB cathodes. For example, lithium carbonates and hydroxides leftover from materials synthesis often contaminate nickel-rich oxide surfaces, which lead to high electrode polarization, reduced first-cycle efficiency, and compromised cell lifetimes.[8–11] Furthermore, during cycling, electrolyte decomposition products, including solvent and salt components from the liquid electrolyte, deposit on and react with the active material surface, forming a solid–electrolyte interphase (SEI).[12–14] Upon repeated cycling, the accumulation of these compounds increases the impedance of the SEI, which is detrimental to electrochemical properties and cyclic stability.

To address the surface impurities formed during materials synthesis, methods such as acid rinsing,[15] aqueous treatments,[16] treatments under vacuum,[17] or electrochemical regeneration[8] have been employed to improve the long-term cycle life of LIBs. Although these methods are effective for research-scale studies on nickel-rich cathode microparticles, they are cumbersome for large-scale materials production and are often ineffective for nanoparticle systems that possess high surface areas and, therefore, greater amounts of impurity species. Additionally, to mitigate the formation of surface degradation products *in operando*, thin surface coating layers have been employed to further stabilize nickel-rich cathode particle surfaces by preventing direct electrode–electrolyte contact while remaining electrochemically inert within the operating voltage window of the cell. In particular, coatings such as $Al_2O_3$,[18] $TiO_2$,[18,19] $SiO_2$,[20] and $Co_3O_4$ (Ref. 21) can be deposited via facile, scalable techniques such as atomic layer deposition or wet chemical methods. However, these strategies are inherently limited by the poor electrical conductivity of the deposited oxide layers.[3] In contrast, a thin, conductive carbon coating (e.g., graphene) can limit the formation of a thick SEI layer and improve charge–discharge kinetics.[7,22] Moreover, since graphene coating schemes minimize the need for additional conductive additives, they are known to increase electrode tap density, which is particularly helpful in overcoming packing density limitations that have traditionally plagued nanoparticle-based electrodes.[23]

Here, we employ surface chemical characterization as a strategy for identifying and minimizing residual hydroxide and carbonate impurities from the synthesis of NCA nanoparticles. Using this surface chemical insight, postsynthetic processing methods are developed to minimize surface impurities and thus improve electrochemical properties. Furthermore, the improved pristineness of the NCA surface facilitates the conformal coating of the NCA nanoparticles with ultrathin conductive and chemically inert graphene. The resulting graphene-coated NCA nanoparticles are then formulated into LIB cathodes, which show superlative electrochemical properties, including low impedance, high rate performance, high volumetric energy and power densities, and long cycling lifetimes. In addition to being directly applicable to emerging nickel-rich LIB cathodes, the methodology presented here can likely be generalized to other LIB electrode materials that are synthesized with hydroxide-based or carbonate-based lithium sources, including oxide-based cathode, anode, and solid-state electrolyte materials.

## II. EXPERIMENTAL DETAILS

### A. Sample preparation

#### 1. NCA synthesis

NCA nanoparticles (nNCAs) were synthesized via a solid-state method. Initially, stoichiometric amounts of nickel (II) acetate tetrahydrate, cobalt (II) acetate tetrahydrate, and aluminum (II) acetate tetrahydrate (Millipore Sigma) were dissolved in de-ionized water to form a 0.1M precursor solution. Oxalic acid dihydrate (Millipore Sigma) was simultaneously dissolved in de-ionized water to form a 0.2M solution. To precipitate the transition metal precursors, the oxalic acid solution was added dropwise to the precursor solution while stirring at 300 rpm to ensure homogeneous mixing. After further stirring for 3 h, the water was evaporated using a rotary evaporator (Buchi Rotavapor R-300 System), yielding the precipitate powder. This powder was then heated in a tube furnace (Thermo Scientific Lindberg Blue M) at 450 °C for 8 h under flowing oxygen. Using a mortar and pestle, the calcined powder was then mixed with lithium hydroxide monohydrate (Millipore Sigma) at a 3 mol. % excess until a homogeneous mixture was formed. The combined powder was calcined at 550 °C for 8 h and then 750 °C for 24 h under flowing oxygen. The refined nanoparticle NCA powder (hereafter referred to as R-nNCA) was obtained by a final heat treatment step at 250 °C under flowing oxygen for 1 h. All furnace ramp rates used were 5 °C/min.

#### 2. Graphene exfoliation

Graphene-ethyl cellulose (EC) powder was produced by shear mixing 150 mesh flake graphite (Millipore Sigma), ethyl cellulose (4 cP, Millipore Sigma), and ethanol (200-proof, Decon Labs) for 2 h at 10 230 rpm using a Silverson L5M-A high shear mixer. The dispersion was then centrifuged for 2 h at 7500 rpm in a Beckman Coulter J26 XPI centrifuge to sediment out large, unexfoliated graphite flakes. The supernatant dispersion was flocculated with a 1M sodium chloride solution at a 9:16 weight ratio (NaCl solution: graphene dispersion) and then centrifuged again at 7500 rpm for 6 min to crash out the graphene-EC powder. These solids were washed with de-ionized water, vacuum filtered, and dried under an infrared lamp. The final graphene fraction in the graphene-EC

powder was 33% as determined by thermogravimetric analysis in air.

### 3. Electrode fabrication

The nNCA electrodes were fabricated by mixing nNCA powder, carbon black (Alfa Aesar), and polyvinylidene fluoride (MTI Corporation) at a 90:5:5 ratio in a mortar and pestle. $N$-methyl pyrrolidone (NMP, Millipore Sigma) was added to form a viscous and homogeneous slurry. The slurry was cast on aluminum foil using a doctor blade, initially dried in a convection oven at 120 °C for 30 min, and subsequently dried in a vacuum oven at 80 °C overnight. This process yielded electrodes with an active material loading of 3 mg/cm$^2$. Electrode discs with 1 cm diameter were cut using a disc cutter and then pressed using a 6 MPa applied pressure prior to coin cell assembly. The R-nNCA electrodes were fabricated using the same method, with the R-nNCA powder serving as the active material. The graphite electrodes for the full cell testing were fabricated using identical methods but used natural graphite powder (Alfa Aesar) as the active material. The graphite slurry was cast on copper foil and dried at 80 °C in the convection oven prior to overnight drying for the full cell experiments.

To form the graphene-coated electrodes, graphene-EC powder and multiwalled carbon nanotubes (MWCNT, MilliporeSigma) were dispersed in ethanol using a horn sonicator (Fisher Scientific Sonic Dismembrator Model 500) equipped with a 1/8 in. tip at 40 W for 1 h. Solvent exchange was performed by adding NMP to this dispersion and evaporating the ethanol using a hot plate set at 80 °C, yielding a dispersion of graphene, ethyl cellulose, MWCNT, and NMP. R-nNCA powder was added to this dispersion to form a viscous slurry, which was mixed homogeneously using a mortar and pestle. The final ratio of solids in this slurry was 95% active material, 4.5% graphene, and 0.5% MWCNT. This ratio was chosen to keep the conductive carbon fraction consistent with the control electrodes made with carbon black. After mixing, the slurry was cast onto aluminum foil and dried in a convection oven set at 120 °C for 30 min and then dried again in a vacuum oven at 80 °C overnight, yielding Gr-R-nNCA electrodes. Electrode discs with a diameter of 1 cm and an active material loading of 3 mg/cm$^2$ were cut and heated to 250 °C for 1 h to decompose the EC. Following thermal decomposition, the electrodes were compressed with a 6 MPa applied pressure prior to coin cell assembly. The Gr-nNCA electrodes were produced using the same method but instead using nNCA powder as the active material.

Electrode thicknesses were measured using a Mitutoyo micrometer. 2032-type coin cells were assembled in an argon glovebox (OMNI-LAB, Vacuum Atmospheres Company) with less than 0.2 ppm of oxygen. For room-temperature testing, Celgard 2325 was used as the separator, and 1M LiPF$_6$ in 1:1 v/v ethylene carbonate/ethyl methyl carbonate (Millipore Sigma) was used as the electrolyte. For low-temperature testing, a polyethylene separator (single-layer PE, Asahi Kasei) and 1M LiPF$_6$ in 1:1 v/v ethylene carbonate/dimethyl carbonate (Millipore Sigma) electrolyte were used. Lithium metal (Alfa Aesar) was used as the counter electrode for half-cell testing. For full-cell testing, graphite electrodes were used as the counter electrode.

### B. Characterization

#### 1. Electrochemical testing

Room-temperature galvanostatic cycling was performed using an Arbin LBT-20084 64-channel battery cycler. For half-cell testing, the NCA electrodes were activated with a constant-current constant-voltage (CCCV) protocol, where the electrode was cycled once at 0.1C with constant-voltage holds at the upper and lower cutoff voltages until the current reached C/20. Here, 1C was set at 200 mAh/g$_{NCA}$. For full-cell testing, the graphite anode was activated with three cycles between 0.01 and 2 V vs Li/Li$^+$ using the same CCCV protocol to form a stable solid–electrolyte interphase on the anode. The graphite electrode was then harvested and assembled in a full cell against an activated NCA cathode. The negative to positive electrode areal capacity ratio (N:P ratio) was set at 1.1:1. Rate capability tests were performed using a charging current rate of 0.1C and then discharging at the desired current rate. Cycle life tests were performed at 1C charge and discharge. Low-temperature testing was performed by cycling the coin cells in an environmental chamber (ESPEC BTX-475) set at 0 °C. Electrochemical impedance spectroscopy tests were conducted in a fully charged state using a Biologic VSP potentiostat between 1 MHz and 100 mHz. The power density was calculated based on the total volume of the electrode and the measured energy at the highest C-rate.

#### 2. Materials characterization

X-ray diffraction (XRD) was conducted on the synthesized powders using a Scintag XDS2000 with Cu Kα (λ = 1.5046 Å) radiation from 10° to 70°. The same analysis was performed on commercially available NCA powder (BASF Toda America). Scanning electron microscopy (SEM) was performed using a Hitachi SU8030 Field Emission SEM at a 5 kV accelerating voltage. SEM samples were prepared by depositing the NCA powder directly onto carbon tape mounted on an SEM stub. Transmission electron microscopy (TEM) samples were prepared by a direct application of the Gr-R-nNCA powder on a lacey carbon supported TEM grid. The TEM imaging was performed using a JEOL ARM 300CF. Raman spectroscopy was conducted using a Horiba Scientific XploRA PLUS Raman microscope with a laser excitation of 532 nm and a laser grating with 1800 grooves/mm. The signal was collected by a 50× LWD Olympus objective (NA = 0.5). X-ray photoelectron spectroscopy (XPS) was performed using a Thermo Scientific ESCALAB 250Xi with Al Kα radiation (∼1486.6 eV). Spectra were acquired after the analysis chamber reached a base pressure of $5 \times 10^{-8}$ Torr. The samples were mounted using copper tape and were charge compensated with a flood gun during acquisition. All spectra were charge corrected to adventitious carbon at 284.8 eV. Postmortem analysis of the battery electrodes was conducted by disassembling the coin cells in an argon glovebox. The harvested electrodes were rinsed with anhydrous dimethyl carbonate (MilliporeSigma) and dried at 120 °C on a hot plate in the glovebox. Postmortem XPS and Raman spectra were acquired using the aforementioned methods.

## III. RESULTS AND DISCUSSION

### A. Surface impurity characterization

Nanoparticles of NCA (hereafter referred to as nNCA) were synthesized using a solid-state method.[24] To validate the quality of the synthesized nNCA, XRD was performed to confirm that the solid-state method yielded NCA with a layered crystal structure [Fig. 1(a)]. The XRD pattern of the synthesized nNCA closely matched the reference pattern obtained from commercial NCA powder and showed no evidence of impurity phases. Furthermore, the splitting of the (006)/(102) peaks and the (018)/(110) peaks provided additional confirmation that the nNCA powder possessed a layered structure. SEM was used to analyze the particle morphology. In contrast to the commercial micrometer-scale powders, the nNCA powder was comprised of primary NCA nanoparticles less than 500 nm in diameter [Figs. 1(b) and 1(c) and S1 in the supplementary material].[39] Together, the XRD and SEM results verified that the solid-state synthesis scheme successfully yielded crystalline NCA nanoparticles.

Although the nNCA powder possessed the desired crystal structure and particle size, a careful analysis of the surface chemistry via XPS revealed that impurity compounds were still present on the surface after synthesis. To deconvolute the XPS C 1s spectra,

four peaks were assigned: C—C bonds at 284.8 eV, C—O bonds at 286.0 eV, C═O bonds at 288.5 eV, and $CO_3$ bonds at 290.7 eV. Similarly, the XPS O 1s spectra were also deconvoluted with four peaks: lattice transition metal–oxygen bonds at 529.2 eV, ROLi species at 530.9 eV, $CO_3$/O—C═O bonds at 531.7 eV, and C—O/ O—C═O bonds at 533.1 eV.[13,25] The C—C bonding nature likely originated from adventitious carbon, while the various carbon–oxygen bond signals can be attributed to the acetate and oxalate precursors used for the nNCA synthesis. On the other hand, the carbonate and ROLi signals are evidence of impurity compounds formed during synthesis.[10]

Since XPS revealed evidence for surface impurity species that can likely be removed through mild heating in an oxidizing environment, postsynthetic annealing treatments were explored to produce a more pristine nNCA surface. In particular, annealing at 250 °C under flowing oxygen gas for 1 h effectively refined the nNCA surface [hereafter referred to as R-nNCA, Fig. 1(d)]. Because heat treatment steps are commonly employed in the existing cathode powder synthesis procedures, this refining step can more easily be implemented in practice compared to other reported strategies for removing surface impurities.[8,15–17] Importantly, this surface refinement step did not lead to any measurable changes to the bulk structure of the nNCA (Fig. S2 in the supplementary
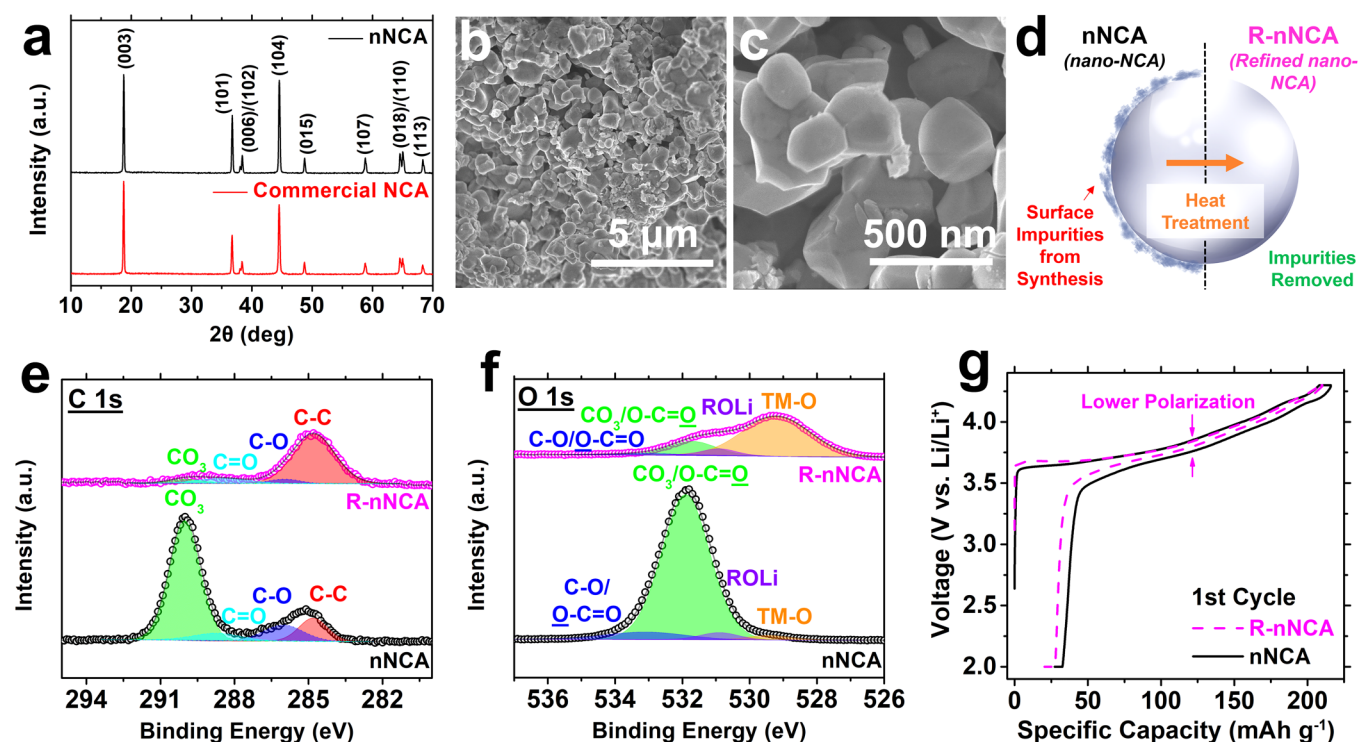


**FIG. 1.** Characterization and control of nanoscale NCA (nNCA) surface chemistry. (a) XRD patterns of nNCA and commercial NCA powder. (b) and (c) SEM images of as-synthesized NCA at different magnifications. (d) Schematic showing the removal of impurities at the NCA particle surface during heat treatment, yielding nanoscale NCA with a refined surface (R-nNCA). (e) C 1s spectra and (f) O 1s spectra of nNCA and R-nNCA powders obtained via XPS. (g) Voltage-capacity plot showing the activation cycles of nNCA and R-nNCA at 0.1C.

material).[39] XPS analysis of the originally synthesized nNCA suggested that the surface possessed a significant carbonate character [Figs. 1(e) and 1(f)], as evidenced by the peaks at 290.7 and 532.1 eV, which is consistent with prior reports.[8–11] In contrast, after the surface refinement step, the XPS C 1s and O 1s spectra of the R-nNCA powder revealed that the intensity of the carbonate peaks decreased dramatically. Additionally, the XPS O 1s spectrum of the R-nNCA powder showed an increase in the peak intensity assigned to lattice transition metal–oxygen bonds at 529.8 eV. This intensity increase is consistent with the removal of a surface layer that would otherwise attenuate the transition metal oxide intensity originating in the particle bulk.

To probe the effect of surface impurities on the electrochemical properties of nNCA, electrochemical cycling measurements were performed on nNCA and R-nNCA samples. Figure 1(g) shows that the R-nNCA electrodes experienced lower electrode polarization during activation than the nNCA electrodes. Since a sample with high electrode polarization reaches its upper cutoff voltage with a higher lithium content than expected, a constant voltage hold allows the electrode to finish delithiating close to its thermodynamically defined lithium content. Therefore, a comparison of the capacity gained during the hold steps at constant voltage serves as a measurement of electrode polarization. In particular, the nNCA electrode gained an additional 7.5 mAh/g of capacity during the constant voltage hold at 4.3 V, corresponding to 3.5% of its charge capacity. In contrast, the R-nNCA electrode only gained 1.6 mAh/g during the voltage hold, corresponding to 0.75% of its charge capacity, which confirms that the surface refinement step did indeed lower the electrode polarization. Moreover, the first cycle efficiency (FCE) for the R-nNCA electrode was 90.4%, whereas the FCE for the nNCA electrode was 87.3%, which shows that the R-nNCA electrode possessed better electrochemical reversibility than the nNCA electrode. This analysis is consistent with prior work, which found that the presence of surface $Li_2CO_3$ species impedes local reaction kinetics near the carbonate deposits.[11] Overall, these results highlight the importance of carefully assessing and controlling the surface chemistry of nickel-rich cathode materials.

## B. Assessing graphene coatings

Surface conductive carbon coating schemes (e.g., conformal graphene coatings) are commonly employed strategies to reduce cell impedance and increase high-rate performance. A solution-phase coating scheme was used to encapsulate the nNCA and R-nNCA particles with a conformal graphene-EC layer, yielding Gr-nNCA and Gr-R-nNCA, respectively [Fig. 2(a)]. The thermal decomposition of the EC polymer leaves behind a carbonaceous residue on the active material surface that possesses a high $sp^2$ character, thus reinforcing the graphitic character of the carbon coating.[22,26] In addition, this residue is highly electrically conductive, thereby improving the electrical contact between adjacent graphene flakes and enhancing electrochemical cycling.[7,22,23,26–29]

Following the coating process, TEM confirmed the presence of a thin carbon layer on the surface of the NCA particles [Figs. 2(b) and 2(c)]. Since this conformal graphene coating scheme yields a highly percolating, electrically conductive network between the

NCA particles, the graphene-coated nNCA (Gr-nNCA) and graphene-coated R-nNCA (Gr-R-nNCA) electrodes were expected to outperform the respective nNCA and R-nNCA control electrodes fabricated with traditional carbon black additives. However, while the Gr-R-nNCA electrode possessed higher initial capacity and better rate capability than the R-nNCA control sample, the Gr-nNCA electrode surprisingly performed considerably worse than the nNCA control electrode [Fig. 2(d)]. This result suggests that an active material surface that is rich in impurity species, such as carbonates, undermines the effectiveness of carbon coating schemes.

Raman spectroscopy and XPS analysis of the pristine electrode surfaces after thermal decomposition of the EC polymer further corroborated that the quality of the electrode coating depends on the cleanliness of the active material surface. The Raman spectra for the Gr-nNCA and Gr-R-nNCA electrodes revealed a large G/D ratio for both samples, which indicated that both electrodes possessed a graphene-like character [Fig. 2(e)]. However, the Gr-nNCA electrode showed greater evidence of an amorphous carbon background than the Gr-R-nNCA electrode, implying that the presence of the carbonate impurities hindered the formation of the $sp^2$-rich carbonaceous residue during the EC thermal decomposition process. Since EC contains many carbon-based and oxygen-based functional groups, evidence of this bonding character in the graphene-coated electrodes would provide further evidence that surface impurities have an adverse impact on EC volatilization.[22] Indeed, the higher relative intensity of the C—O peak in the XPS C 1s spectrum of the Gr-nNCA electrode compared to the Gr-R-nNCA electrode confirms the difference in amorphous carbon signals between the two electrodes [Fig. 2(f)]. Furthermore, the XPS C 1s and O 1s spectra [Figs. 2(f) and 2(g)] of the Gr-nNCA electrode showed a much higher carbonate signal than the Gr-R-nNCA electrode, suggesting that these species persisted through the second heat treatment step where the EC polymer is supposed to be decomposed. Since the carbonate species are detrimental to electrochemical cycling, these spectroscopic data are consistent with the electrochemical results that showed the poorest performance for the Gr-nNCA electrode.

## C. Comparative electrochemical characterization

To further assess the combined advantages of surface refinement and conformal graphene coating, additional electrochemical characterization was undertaken. For example, Fig. 3(a) shows that surface refinement coupled with the conformal graphene coating significantly improved the cycle life of the NCA material. After 200 cycles at a 1C cycling rate, the Gr-R-nNCA electrode possessed a capacity of 91.8 mAh/g, corresponding to 60.5% capacity retention. In contrast, the nNCA control electrode degraded quickly within the first 100 cycles, ultimately resulting in a capacity of 21.2 mAh/g after 200 cycles, corresponding to 15.9% capacity retention.

Over 200 cycles, the nNCA electrode possessed an average Coulombic efficiency of 98.56%, which was marginally higher than the 98.52% average efficiency for the Gr-R-nNCA electrode. Although these average values were similar in magnitude, the Coulombic efficiency for the Gr-R-nNCA electrode was significantly more stable than that of the nNCA electrode [Fig. 3(a)]. The
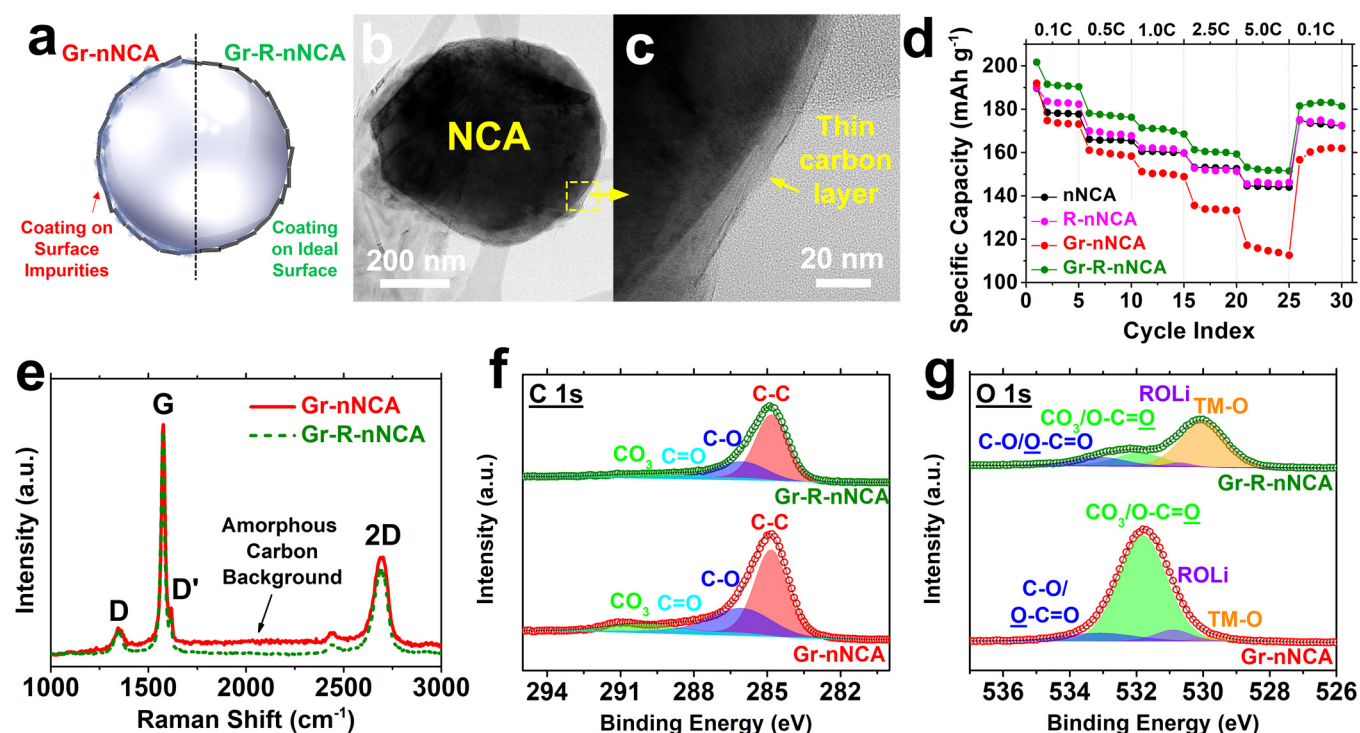
**FIG. 2.** Results for conformal graphene coatings. (a) Schematic showing that a conformal graphene coating will encapsulate surface impurities on nNCA (Gr-nNCA), in contrast to a conformal graphene coating on a refined, impurity-free surface (Gr-R-nNCA). (b) and (c) TEM images showing the surface of the Gr-R-nNCA particles. (d) Half-cell rate capability test of nNCA, R-nNCA, Gr-nNCA, and Gr-R-nNCA electrodes. (e) Raman spectra for Gr-nNCA and Gr-R-nNCA. (f) C 1s spectra and (g) O 1s spectra of Gr-nNCA and Gr-R-nNCA obtained via XPS.

large fluctuations in the nNCA Coulombic efficiency values suggested variations in lithium consumption during each cycle, which could be a by-product of unstable interfacial layers on the nNCA particle surface. If the SEI is fragile and breaks down with each cycle, additional lithium must be consumed to reform the interphase. In contrast, the Coulombic efficiency evolution for the Gr-R-nNCA electrode remains stable throughout 200 cycles, which is consistent with the superior cycle life observed for the Gr-R-nNCA electrode.

To elucidate the origins of the observed cycle life improvement, postmortem XPS analysis of the cathode surfaces was performed. The XPS O 1s spectra for the Gr-R-nNCA and nNCA samples were fit with the same four component spectra as the pristine electrodes, as well as an additional peak at 534.7 eV that was assigned to $Li_xPO_yF_z$ species formed *in operando* due to electrolyte decomposition [Fig. 3(b)].[13,30] For the nNCA electrode after cycling, the increase in the C—O and C=O spectral peaks, the clear presence of $Li_xPO_yF_z$ species, the changes in the Ni 2p spectrum compared to the pristine electrode [Fig. 3(c) and S3 in the supplementary material],[39] and the absence of any discernable Co 2p signal [Fig. 3(d) and S3 in the supplementary material][39] together suggest that the nNCA surface was coated with a layer during cycling that is rich in organic and fluorophosphate

components. The formation of this layer is well known and has been attributed to a ring-opening reaction of the ethylene carbonate solvent, which is assisted by transition metal ions on the cathode surface.[13] Other reported degradation reactions, such as transition metal etching by trace amounts of HF in the electrolyte,[31] may also contribute to the surface degradation in the nNCA electrode.

In contrast, fewer changes were observed for the Gr-R-nNCA electrode after cycling. Although some slight increases in the carbon–oxygen bond intensities are observed in the XPS C 1s and O 1s spectra, little evidence exists for fluorophosphate degradation products [Fig. 3(b) and S4 in the supplementary material].[39] Furthermore, the transition metal oxide signal and the minimal changes in the Ni 2p and Co 2p spectral features for the pristine and postmortem electrodes [Figs. 3(c) and 3(d) and S3 in the supplementary material][39] suggest that the Gr-R-nNCA surface did not significantly degrade during cycling. Postmortem Raman spectroscopy of the Gr-R-nNCA electrode also corroborated this conclusion (Fig. S5 in the supplementary material).[39] If electrochemical cycling had altered the integrity of the graphene coating, then the increased defect density in the graphene coating would have resulted in a decrease of the G/D ratio. Even after 200 charge-discharge cycles, the Raman spectrum for the Gr-R-nNCA
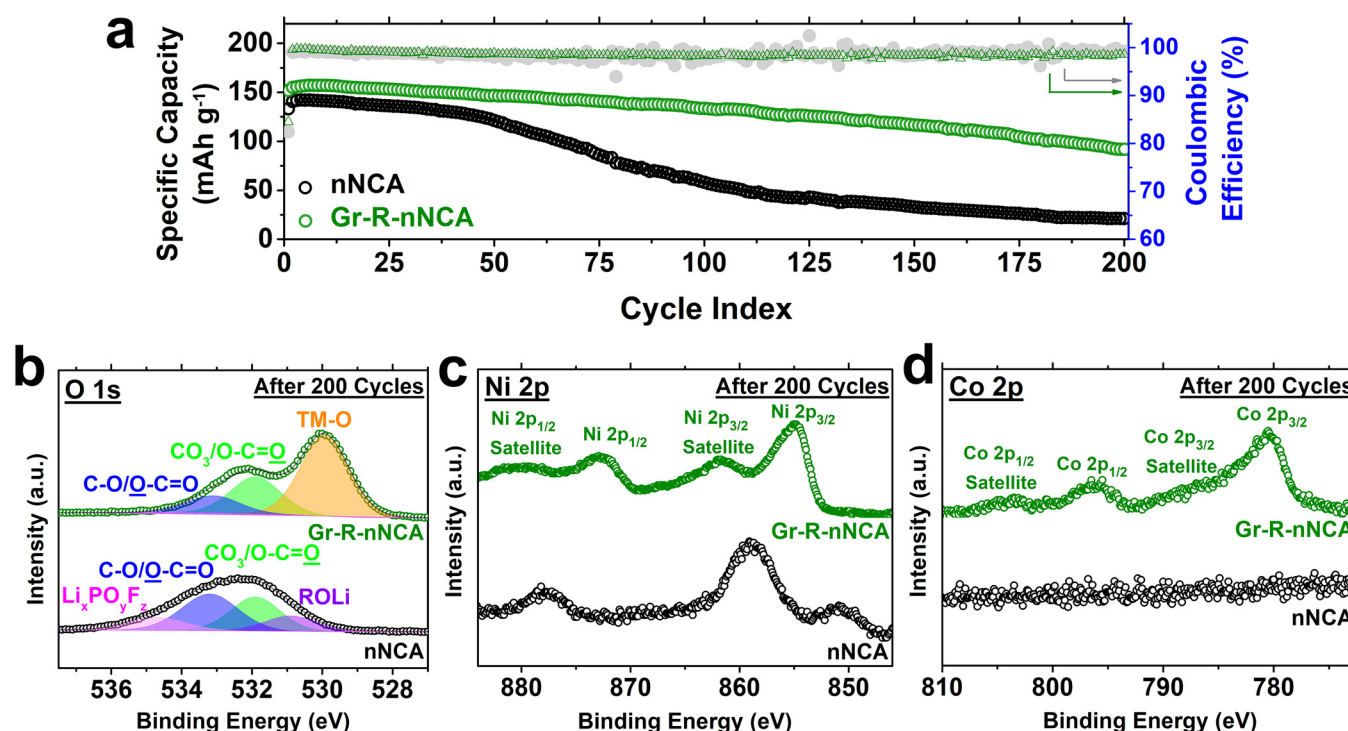
FIG. 3. Graphene-coated nanoscale NCA exhibits improved cycle life compared to the control. (a) Half-cell cycle life test at 1C. (b) O 1s, (c) Ni 2p, and (d) Co 2p postmortem XPS spectra show significant evidence of degradation for the uncoated nNCA electrode.

electrode continues to exhibit a large G/D ratio, which confirms that the electrode maintained its graphene-like character throughout the cycle life test. Small changes in the amorphous carbon background are likely due to organic electrolyte degradation products, which are also present in the XPS C 1s spectrum. Similar to other electrode coating schemes,[18–21] the conformal graphene coating in the Gr-R-nNCA electrode apparently acts as a barrier layer that minimizes the interaction between the transition metals in the active material and the electrolyte, effectively mitigating the severity and extent of electrolyte decomposition. Additionally, the graphene coating may act as a scavenger for HF, which would otherwise etch the transition metals near the surface and degrade interfacial charge transport.

The combination of surface refinement and conformal graphene coating enabled substantial enhancements in numerous other electrochemical performance metrics. Prior work has shown that graphene-coated microparticle electrodes experienced large improvements in volumetric capacity due to the replacement of low-density carbon black with a percolating graphene network.[23] Here, the initial volumetric capacities again reflected this phenomenon for nickel-rich nanoparticles. Specifically, the Gr-R-nNCA electrode reached an initial volumetric discharge capacity of 412.6 mAh/cm$^3$, while the nNCA electrode only reached an initial volumetric discharge capacity of 311.7 mAh/cm$^3$ [Fig. 4(a)]. The high electrical conductivity of the graphene network also promotes fast electronic transport, while the nanoparticle NCA morphology

provides short Li-ion diffusion lengths into the bulk and increases the number of charge transfer reaction sites. Together, these factors significantly improved the high-rate performance of the Gr-R-nNCA electrode compared to the nNCA control sample. When discharged at 15C, the Gr-R-nNCA electrode possessed a volumetric capacity of 273 mAh/cm$^3$, while the volumetric capacity of the nNCA control electrode dramatically dropped to 78.5 mAh/cm$^3$. Electrochemical impedance spectroscopy was also performed on the electrodes after cycling at different current rates to confirm the enhancement in charge transport behavior. The Nyquist plots showed that the Gr-R-nNCA electrode possessed substantially lower cell impedance (~5 Ω) than the nNCA electrode (~15 Ω), thereby corroborating the rate capability results [Fig. 4(b)].

To test the limits of the Gr-R-nNCA electrode, full cells were assembled and subjected to galvanostatic cycling at 0 °C. Under these conditions, the amount of lithium in the full cell is restricted to the capacity possessed by the cathode, implying that parasitic side reactions that irreversibly consume lithium become even more deleterious. Furthermore, ionic charge transport is more sluggish at low temperatures, which reduces discharge capacities, particularly at high applied current rates. Despite these harsh testing conditions, the Gr-R-nNCA|Graphite full cell showed impressive electrochemical performance. Specifically, at all current rates, the Gr-R-nNCA|Graphite full cell possessed higher capacities than the nNCA|Graphite full cell [Fig. 4(c)]. The Nyquist plot further showed that the lower impedance observed in the half-cell
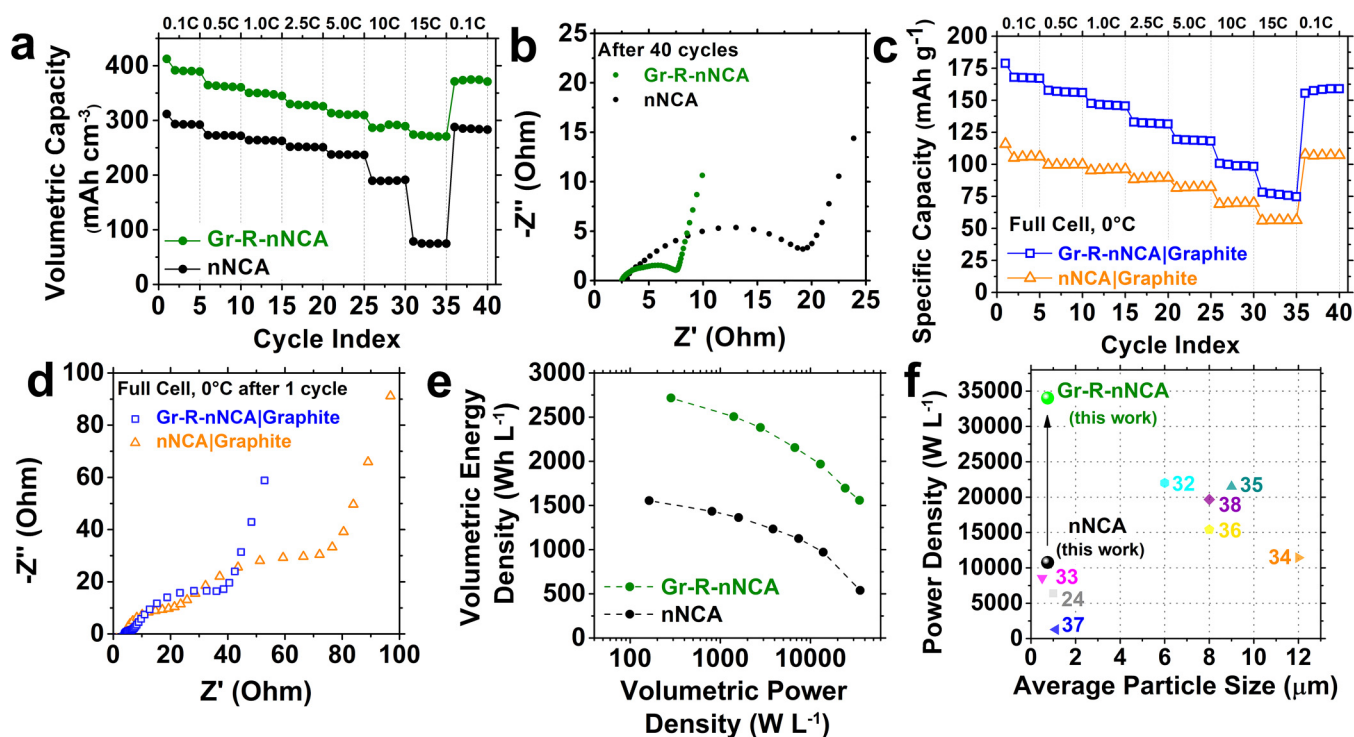
**FIG. 4.** Electrochemical testing shows that graphene-coated Gr-R-nNCA electrodes enable comprehensive performance improvements compared to the nNCA control. (a) Half-cell volumetric rate capability test. (b) Nyquist plot of the electrodes at room temperature. (c) Full-cell rate capability test at 0 °C. (d) Nyquist plot of the full cells at 0 °C. (e) Ragone plot showing the improved power and energy density of the Gr-R-nNCA electrode. (f) Plot showing the power density competitive advantage of Gr-R-nNCA electrodes compared to the literature precedent. The numbers indicate the references for previously reported results.

geometry tested at room temperature was again evident for the full cell at 0 °C [Fig. 4(d)]. The smaller high-frequency arcs for the Gr-R-nNCA|Graphite sample suggest that both the surface film and charge transfer impedances were lower than the nNCA control sample, indicating that interfacial charge transport was significantly improved by the graphene coating.

The high volumetric capacity and superlative rate capability enabled by the surface refinement and subsequent conformal graphene coating correspondingly led to substantial improvements in the energy and power densities. These enhancements are evident on a Ragone plot [Fig. 4(e)], which shows that the Gr-R-nNCA sample clearly outperformed the nNCA control sample. Additionally, the exceptionally high volumetric power density for the Gr-R-NCA sample compares favorably to the literature precedent for NCA-based cathodes [Fig. 4(f)].[24,32–38] Overall, these results establish that Gr-R-nNCA cathodes enable high-performance LIBs with long cell lifetimes, high rate capability, and wide operating temperature windows.

## IV. SUMMARY AND CONCLUSIONS

In summary, we have explored the surface chemistry of nanoscale nickel-rich cathode particles to identify and remove residual contaminants from solid-state synthesis. The resulting chemically

pristine nanoparticles were more amenable to a conformal graphene coating, ultimately resulting in a nanoparticle-based electrode with exceptional electrochemical properties. Specifically, the surface refinement and conformal graphene coating enabled superlative performance in LIBs including high rate capability, low impedance, high volumetric energy and power densities, and long cycle life. In addition, these nanostructured cathode materials widened the LIB operating range, particularly at low temperatures. While demonstrated here for nickel-rich LIB cathodes, this methodology can likely be generalized to other energy storage electrodes, such as sodium-ion or magnesium-ion batteries, that incorporate nanostructured materials possessing a high surface area. Therefore, this work establishes a clear path forward for the realization of high-performance, nanoparticle-based energy storage devices.

## AUTHORS' CONTRIBUTIONS

J.-M.L. and N.S.L. contributed equally to this work.

## ACKNOWLEDGMENTS

## REFERENCES

[1]W. Li, E. M. Erickson, and A. Manthiram, Nat. Energy 5, 26 (2020).
[2]S. T. Myung, F. Maglia, K. J. Park, C. S. Yoon, P. Lamp, S. J. Kim, and Y. K. Sun, ACS Energy Lett. 2, 196 (2017).
[3]Y. Xia, J. Zheng, C. Wang, and M. Gu, Nano Energy 49, 434 (2018).
[4]Y. Talyosef, B. Markovsky, R. Lavi, G. Salitra, D. Aurbach, D. Kovacheva, M. Gorova, E. Zhecheva, and R. Stoyanova, J. Electrochem. Soc. 154, A682 (2007).
[5]J. Collins, G. Gourdin, M. Foster, and D. Qu, Carbon 92, 193 (2015).
[6]J. Collins, J. P. de Souza, M. Hopstaken, J. A. Ott, S. W. Bedell, and D. K. Sadana, IScience 23, 101586 (2020).
[7]K. S. Chen et al., Nano Lett. 17, 2539 (2017).
[8]C. Wang et al., ACS Appl. Mater. Interfaces 11, 44036 (2019).
[9]G. V. Zhuang, G. Chen, J. Shim, X. Song, P. N. Ross, and T. J. Richardson, J. Power Sources 134, 293 (2004).
[10]S. E. Renfrew and B. D. McCloskey, J. Am. Chem. Soc. 139, 17853 (2017).
[11]A. Grenier, H. Liu, K. M. Wiaderek, Z. W. Lebens-Higgins, O. J. Borkiewicz, L. F. J. Piper, P. J. Chupas, and K. W. Chapman, Chem. Mater. 29, 7345 (2017).
[12]M. Gauthier et al., J. Phys. Chem. Lett. 6, 4653 (2015).
[13]Y. Yu, P. Karayaylali, Y. Katayama, L. Giordano, M. Gauthier, F. Maglia, R. Jung, I. Lund, and Y. Shao-Horn, J. Phys. Chem. C 122, 27368 (2018).
[14]L. Giordano, P. Karayaylali, Y. Yu, Y. Katayama, F. Maglia, S. Lux, and Y. Shao-Horn, J. Phys. Chem. Lett. 8, 3881 (2017).
[15]S. Ramakrishnan, B. Park, J. Wu, W. Yang, and B. D. McCloskey, J. Am. Chem. Soc. 142, 8522 (2020).
[16]S. E. Renfrew, L. A. Kaufman, and B. D. McCloskey, ACS Appl. Mater. Interfaces 11, 34913 (2019).
[17]J. C. Jones, S. Rajendran, A. Pilli, V. Lee, N. Chugh, L. M. R. Arava, and J. A. Kelber, J. Vac. Sci. Technol. A 38, 023201 (2020).
[18]D. Mohanty et al., Sci. Rep. 6, 26532 (2016).
[19]G. Dai, H. Du, S. Wang, J. Cao, M. Yu, Y. Chen, Y. Tang, A. Li, and Y. Chen, RSC Adv. 6, 100841 (2016).
[20]Y. Cho and J. Cho, J. Electrochem. Soc. 157, A625 (2010).
[21]Y. Huang, Y. Huang, and X. Hu, Electrochim. Acta 231, 294 (2017).
[22]J.-M. Lim et al., Matter 3, 522 (2020).
[23]K. Y. Park et al., Adv. Energy Mater. 10, 2001216 (2020).
[24]Z. Qiu, Y. Zhang, P. Dong, S. Xia, and Y. Yao, Solid State Ionics 307, 73 (2017).
[25]R. T. Haasch and D. P. Abraham, Surf. Sci. Spectra 26, 014003 (2019).
[26]E. B. Secor, P. L. Prabhumirashi, K. Puntambekar, M. L. Geier, and M. C. Hersam, J. Phys. Chem. Lett. 4, 1347 (2013).
[27]E. B. Secor, T. Z. Gao, A. E. Islam, R. Rao, S. G. Wallace, J. Zhu, K. W. Putz, B. Maruyama, and M. C. Hersam, Chem. Mater. 29, 2332 (2017).
[28]E. B. Secor, T. Z. Gao, M. H. Dos Santos, S. G. Wallace, K. W. Putz, and M. C. Hersam, ACS Appl. Mater. Interfaces 9, 29418 (2017).
[29]A. E. Baumann, J. R. Downing, D. A. Burns, M. C. Hersam, and V. S. Thoi, ACS Appl. Mater. Interfaces 12, 37173 (2020).
[30]R. Dedryvère, H. Martinez, S. Leroy, D. Lemordant, F. Bonhomme, P. Biensan, and D. Gonbeau, J. Power Sources 174, 462 (2007).
[31]X. Yang et al., J. Mater. Chem. A 6, 16149 (2018).
[32]M. J. Lee, M. Noh, M. H. Park, M. Jo, H. Kim, H. Nam, and J. Cho, J. Mater. Chem. A 3, 13453 (2015).
[33]Y. Li, H. Yu, Y. Hu, H. Jiang, and C. Li, J. Energy Chem. 27, 559 (2018).
[34]X. He, X. Xu, L. Wang, C. Du, X. Cheng, P. Zuo, Y. Ma, and G. Yin, J. Electrochem. Soc. 166, A143 (2019).
[35]C. H. Lai, D. S. Ashby, T. C. Lin, J. Lau, A. Dawson, S. H. Tolbert, and B. S. Dunn, Chem. Mater. 30, 2589 (2018).
[36]N. Wu, H. Wu, W. Yuan, S. Liu, J. Liao, and Y. Zhang, J. Mater. Chem. A 3, 13648 (2015).
[37]K. S. Ryu, S. H. Lee, B. K. Koo, J. W. Lee, K. M. Kim, and Y. J. Park, J. Appl. Electrochem. 38, 1385 (2008).
[38]J. H. Shim, Y. M. Kim, M. Park, J. Kim, and S. Lee, ACS Appl. Mater. Interfaces 9, 18720 (2017).
[39]See supplementary material at https://doi.org/10.1116/6.0000580 for additional electron microscopy, x-ray diffraction, x-ray photoelectron spectroscopy, and Raman spectroscopy data.

## Biography

**Mark C. Hersam** is the Walter P. Murphy Professor of Materials Science and Engineering and Director of the Materials Research Center at Northwestern University. He also holds faculty appointments in the Departments of Chemistry, Applied Physics, Medicine, and Electrical Engineering. He earned a B.S. in Electrical Engineering from the University of Illinois at Urbana-Champaign (UIUC) in 1996, M.Phil. in Physics from the University of Cambridge (UK) in 1997, and a Ph.D. in Electrical Engineering from UIUC in 2000. His research interests include nanomaterials, nanomanufacturing, scanning probe microscopy, nanoelectronic devices, biosensors, and renewable energy. Dr. Hersam has received several honors including the Presidential Early Career Award for Scientists and Engineers (2005), TMS Robert Lansing Hardy Award (2006), AVS Peter Mark Award (2006), MRS Outstanding Young Investigator (2010), MacArthur Fellowship (2014), U.S. Science Envoy (2016), AVS Nanotechnology Recognition Award (2016), AVS Medard W. Welch Award (2020), and eight Teacher of the Year Awards. An elected member of the National Academy of Inventors, Dr. Hersam has founded two companies, NanoIntegris and Volexion, which are commercial suppliers of nanoelectronic and battery materials, respectively. Dr. Hersam is a Fellow of MRS, AVS, APS, AAAS, SPIE, and IEEE and also serves as an Associate Editor of *ACS Nano*.